ADVANCED INTELLIGENT SYSTEMS
Open Access
www.advintellsyst.com

Large-Scale Surface Shape Sensing with Learning-Based Computational Mechanics

*Kui Wang, Chi-Hin Mak, Justin D. L. Ho, Zhiyu Liu, Kam-Yim Sze, Kenneth K. Y. Wong, Kaspar Althoefer, Yunhui Liu, Toshio Fukuda, and Ka-Wai Kwok**

Proprioception, the ability to perceive one's own configuration and movement in space, enables organisms to safely and accurately interact with their environment and each other. The underlying sensory nerves that make this possible are highly dense and use sophisticated communication pathways to propagate signals from nerves in muscle, skin, and joints to the central nervous system wherein the organism can process and react to stimuli. In a step forward to realize robots with such perceptive capability, a flexible sensor framework that incorporates a novel modeling strategy, taking advantage of computational mechanics and machine learning, is proposed. The sensor framework on a large flexible sensor that transforms sparsely distributed strains into continuous surface is implemented. Finite element (FE) analysis is utilized to determine design parameters, while an FE model is built to enrich the morphological data used in the supervised training to achieve continuous surface reconstruction. A mapping between the local strain data and the enriched surface data is subsequently trained using ensemble learning. This hybrid approach enables real time, robust, and high-order surface reconstruction. The sensing performance is evaluated in terms of accuracy, repeatability, and feasibility with numerous scenarios, which has not been demonstrated on such a large-scale sensor before.

1. Introduction

Proprioception plays a fundamental part in biological systems, allowing precise and safe interaction with their environment. In the landscape of bioinspired technologies, proprioceptive awareness plays a similar role, allowing robots to effectively explore unstructured environments and ensure safe interaction.[1,2] Basic proprioception in robotics has been developed in the form of joint encoders and pressure sensors but is lacking in the detection of higher order morphological changes. With the advancement of flexible robotic systems, including soft robotics, the task of integrating proprioception becomes challenging when compared with their standard rigid-link counterparts. In particular for soft robots, their conformability and infinite degrees of freedom (DoF) allow them to perform challenging tasks but pose additional complications for their proprioception due to often unrestricted deformability.[3,4] This not only raises an additional challenge above rigid-link robots, as sensing possibilities for soft robotics are not limited to robot tip position or simplified curves, but also extends to detecting 3D surface shape to fully represent their morphology.[5]

In the past, researchers have realized surface shape sensing by using dense arrays of sensors.[6] These sensor arrays could gather local position and orientation information, combining to give global displacement profiles and therefore shape reconstruction. Microelectromechanical systems (MEMS) in various forms are commonly integrated with robotic systems.[7,8] These small-sized sensors can be attached to objects

K. Wang, C.-H. Mak, J. D. L. Ho, Z. Liu, K.-Y. Sze, K.-W. Kwok
Department of Mechanical Engineering
The University of Hong Kong
Hong Kong, P. R. China
E-mail: kwokkw@hku.hk

K. K. Y. Wong
Department of Electrical and Electronic Engineering
The University of Hong Kong
Hong Kong, P. R. China

The ORCID identification number(s) for the author(s) of this article can be found under https://doi.org/10.1002/aisy.202100089.

© 2021 The Authors. Advanced Intelligent Systems published by Wiley-VCH GmbH. This is an open access article under the terms of the Creative Commons Attribution License, which permits use, distribution and reproduction in any medium, provided the original work is properly cited.

DOI: 10.1002/aisy.202100089

K. Althoefer
School of Electronic Engineering and Computer Science
Queen Mary University of London
London E1 4NS, UK

Y. Liu
Department of Mechanical and Automation Engineering
The Chinese University of Hong Kong
Hong Kong, P. R. China

T. Fukuda
Department of Micro-Nano Systems Engineering
Nagoya University
Nagoya 464-8601, Japan

for transducing local position and orientation information. A similar design can be seen in grid-patterned, three-axis accelerometers attached on a surface[9,10] and an artificial skin with a rigid hexagonal sensor as the unit cell.[11] These cells communicate their relative poses with each other to generate the overall surface shape. Saguin-Sprynski extended the work to a sparsely distributed sensor array.[12] The surface curves as well as orientation measurements were utilized for surface shape reconstruction. However, the complexity of wiring and electrical connections severely hinders scalability and compatibility with flexible robotic systems. Some efforts have been dedicated to using an optical-based method to estimate surface shape. Through multiplexing small-sized and compliant optical sensors,[13–15] wiring complexity is highly reduced. For instance, in work done by Xu et al., two fiber layers were used in a mesh layout to detect 3D shapes.[16] However, this type of design requires precise orthogonal alignment of two fiber layers to sense and reconstruct both convex and concave shapes.

Compared with precisely and densely laid sensor layouts, researchers began to search for solutions requiring fewer local sensing elements and lower configuration complexity.[3,6] As a result, data-driven methods have been proposed. For instance, Rendl et al. printed 16 piezoelectric sensors at an outer ring of a transparent sheet, for sensing continuous surface deformations.[17] This provided a flexible system that could sense the bending configuration with roughly centimeter-level accuracy over an A4-like form-factor, using a machine learning approach. In other research, an array of optical fiber was embedded inside an elastomeric foam, with their outputs fed to several machine learning algorithms to predict the sensor deformation mode and angle.[18] In our previous work, a square surface shape sensor was designed, wherein a dual-layer fiber Bragg grating (FBG) layout was embedded in a silicone rubber substrate and a neural network was implemented for real-time 3D shape reconstruction.[19] However, the small size ($45 \times 45 \times 5$ mm) of the sensor, to some degree, limited the deformation magnitude and its range of applications. Generally, these reconstruction methods dealt well with sensing simple morphology changes. However, challenges include limited sensing ability for complex and large-scale deformation, as well as dependence on sufficient training data acquired physically with larger sizes of sensors.

Representation of irregular or complicated surfaces remains challenging, especially for large-scale target and dynamic morphology changes. The finite element (FE) method can provide high accuracy and sufficient virtual data,[20] as it takes geometric and material characteristics into account.[21] As FE modeling can provide abundant noise-free data, it is an interesting proposition to train a learning-based model with such virtually generated data.[22] Previously, Lee et al. proposed a nonparametric model learning framework for controlling a hydraulic-driven soft robot.[23] In their study, pretraining data are obtained by sampling data from a FE model for initializing an online kinematics model. However, the high computational costs associated with the numerical analysis usually confined it to be used offline only. To speed up the FE simulation for real-time applications, several techniques have been proposed.[20] One approach is to lower the computational complexity of the algorithm through a reduction of the model's DoF. However, this method would result in a loss of accuracy, especially for models with high nonlinearity. Another speed-up approach is to use parallel computing strategies by dividing the global complex problem domain into smaller independent subdomains processed simultaneously;[24] however, it is still far from enabling high-frequency FE simulation in real time.

To realize accurate and real-time proprioception, we propose a real-time surface sensing framework applicable to various sensor shapes and sensing element types. The framework integrates FE modeling with machine learning methods, requiring only sparsely distributed sensing elements to predict dynamic and complicated morphology changes in the sensor. Such integration provides basis for the development of large-scale shape sensing, which has not been demonstrated and reported before. The proposed shape sensing frame could be used as a wearable device or on some bioinspired robots, such as marine robot[25,26] and flying soft robot.[27] FE analysis is used to analyze sensor parameters and to enrich machine learning training data by generating a dense array of enriched nodes from a much smaller set of tracked nodes. Using this approach, we can effectively compensate for accumulated errors and provide robust surface shape reconstruction. We propose an ensemble learning model comprising 24 artificial neural networks (ANNs) to learn and train the strain-to-shape mapping. To ensure real-time prediction, the calculation time is limited to 10 ms in each time step. The primary contributions of this research are differentiated as follows: 1) Development of a surface sensing framework that is validated on a large-scale (e.g., A4-sized), flexible, and thin (1 mm) sensor prototype capable of undergoing high-order surface deformation in real time. 2) A learning-based morphology modeling approach using FE-enriched data, which enables application-focused customization and production. 3) Experimental verification for the proposed shape reconstruction is conducted to characterize the sensor accuracy, flexibility, and repeatability, even being displaced by hydrodynamic forces.

2. Results and Discussion

An A4-sized (210×297 mm) flexible surface shape sensor (**Figure 1**) was developed through our FE-integrated framework (Figure S1, Supporting Information). FE modeling is utilized for testing design parameters of the sensor prior to fabrication, wherein parameters such as sensor thickness and sensing element placement can be tuned depending on the intended application. The surface shape sensor utilized 29 sparsely distributed FBGs as the underlying sensing elements for measuring strain, which were subsequently used as inputs to train a model to reconstruct the 3D surface morphology of the shape sensor. A demonstration of the shape sensor's response to different external stimuli is presented in Video S1 and S2, Supporting Information, including shape reconstruction during hands-on deformation, and impact from water jet and small projectile beads. Shape reconstruction accuracy, repeatability, and hysteresis tests were also performed on the developed shape sensor. The resulting performance is achieved through our hybrid approach of FE-based data enrichment and ensemble learning method, with details described in the sections later.

© 2021 The Authors. Advanced Intelligent Systems published by Wiley-VCH GmbH

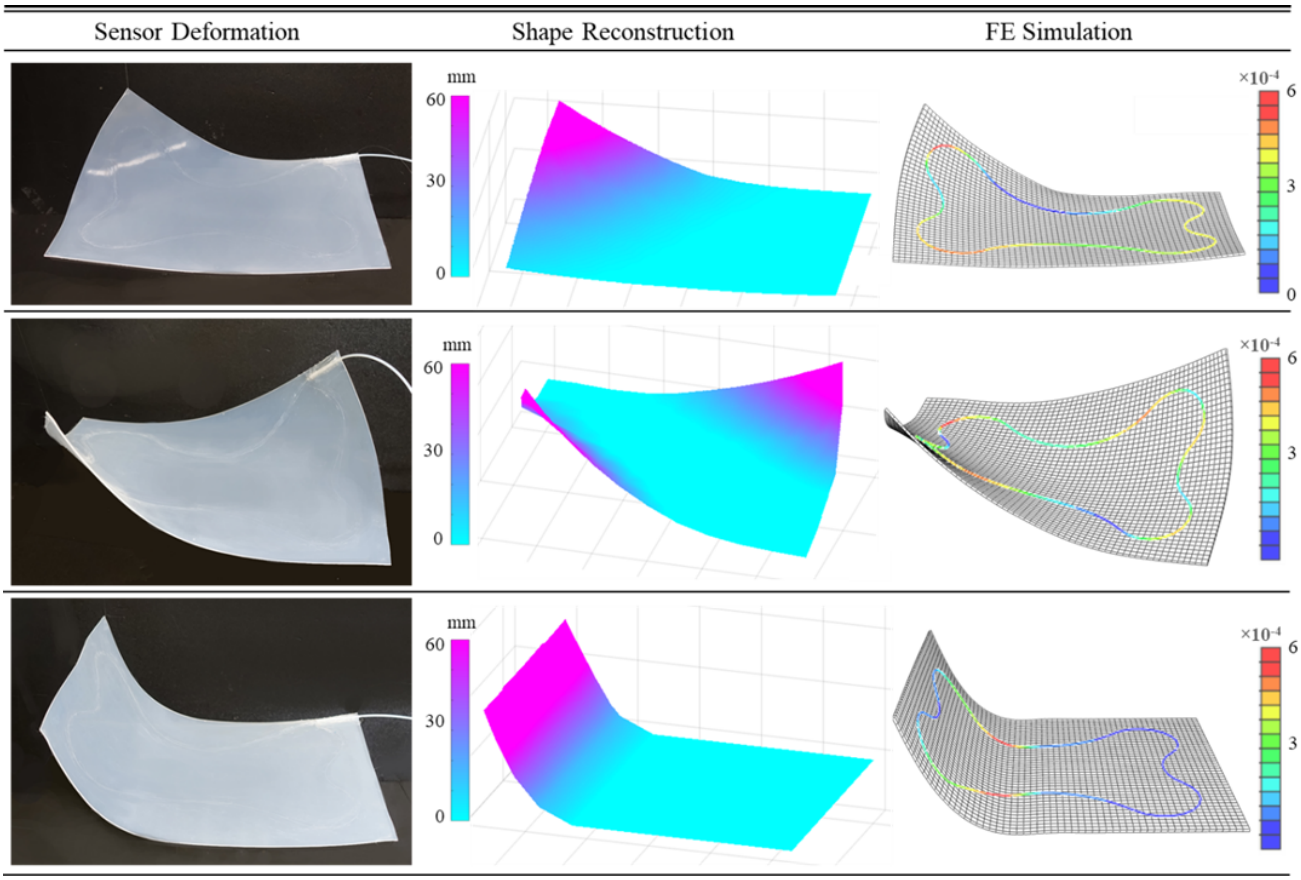

Figure 1. Surface shape reconstruction instances. The deformed shape sensor (left column) is illustrated with corresponding shape reconstruction (middle column) with warmer colors indicating larger displacement (see Video S1 and S2, Supporting Information). FE simulations with fiber placement (right column) are shown with colored lines, indicating the magnitude of fiber strain.

2.1. Morphology Reconstruction via Ensemble Learning

Proprioception in real time typically requires high update frequency and low latency while minimizing compromise on sensing accuracy. To achieve high-frequency calculation, an ensembled model was used to create a mapping from the 29 FBG strain data to a grid of 11×7 surface node positions evenly distributed along the shape sensor (**Figure 2**a).

Ground truth data were obtained by capturing the 3D position of nine control points selected on the shape sensor surface, which were distributed evenly along its four edges, along with one located in the center. During the data capture, one corner control point was fixed in position and the remaining eight control points were each measured at 40 Hz with five DoF electromagnetic (EM) tracking markers (Aurora V3, NDI) attached to the shape sensor surface (Figure 2a), while the FBG strain data were simultaneously captured (FBG-Scan 804D).

All the data for model training were obtained in a single session of hands-on sensor deformation, which took over 100 s and ≈20 different "key-frame" poses. The nine tracked control points were enriched to a grid of 11×7 positional nodes through FE-based data enrichment, and then used for the ensemble model output. The 29 strain-measuring FBGs were integrated into the shape sensor in a single optical fiber placed in a dog-bone layout (Figure 2a), with center-to-center spacings of ≈22 mm between FBGs. A total of 1500 sets of FBG and node data were captured, with 1000 used for training the learning model, 200 for model validation, and 300 for testing of reconstruction accuracy. To withstand repeated strains sensing, we intentionally kept a safety threshold of bending radius during data acquisition. Extreme robot configurations that induce large local strains were avoided, and the resulting valid minimum sensing bending radius is ≈20 mm.

Ensemble learning configuration parameters in terms of 1) the node density (total nodes in the A4 size) and 2) the submodel size (window size) were tested to evaluate their effect on prediction accuracy and processing time. As shown in Figure 2b, three different node densities (i.e., 7×5, 11×7, and 21×13 nodes) and eight window sizes (ranging from 1/16 to 1 times the A4 size) were compared. As for a specified node density, smaller window sizes would result in more windows (submodels) for prediction, thereby increasing the processing time. It also reduces the prediction error, which refers to hereinafter as the deviation between the predicted nodal displacement and the EM-tracked displacement. The denser the node on the A4, the longer the prediction time due to the increased

© 2021 The Authors. Advanced Intelligent Systems published by Wiley-VCH GmbH

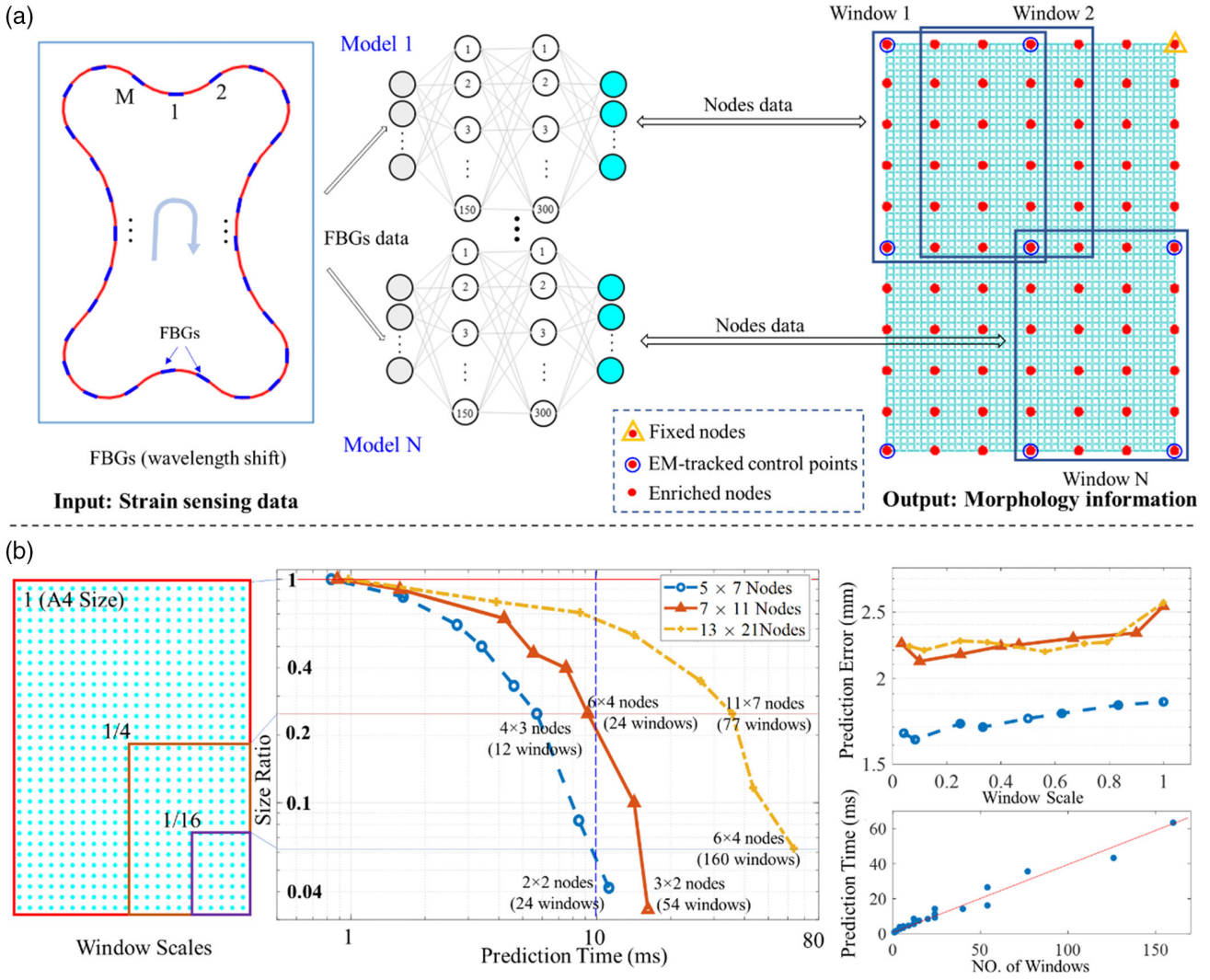

Figure 2. Model training with ensemble learning. a) Model training with *M* Bragg shifted wavelengths as input to *N* (6 × 4) multilayer Perceptron regressors, which includes two hidden layers of 150 and 300 neurons, respectively. The whole surface node set is divided by *N* windows, with each window covering the same number of nodes. Each window involves an ANN-based submodel with the same *M* (29) input FBGs data. b) Prediction time and accuracy as a result of changing the node density (7 × 5, 11 × 7, and 21 × 13 nodes) and the window size (from 1/16 to 1 times the A4 size), where the size ratio refers to the ratio of window size to the A4 size.

number of submodels as well as the higher output data size for each submodel. To maintain a reasonably high update frequency at >100 Hz required for closed-loop robotic control, we limit the processing time per time step <10 ms. This is also a requirement for neural transmission when realizing proprioception, which takes in a few milliseconds or less. Therefore, 11 × 7 nodes with 24 submodels (6 × 4 nodes) were selected for this A4-size surface model training (i7-6820HK, 16 GB RAM, GTX 1070), taking account of a trade-off among the FE-based nodes density, the learning-based prediction error, and the sensing frequency.

2.2. FE-Based Data Enrichment

The integration of FE-based data enrichment highly relaxes the amount of ground truth that needs to be captured in a data-driven approach, where position-tracked control points data were imported into the FE model as displacement constraints to generate a rich amount of surface nodes data offline. Although we utilized an EM-based tracking system for ground truth capturing, other tracking modalities can be used with this sensing framework, provided that they are capable of accurately measuring node data on the shape sensor surface even in the case of complex or overlapping deformation. For example, camera-based motion capture systems can be used to obtain the original node data and then become enriched via FE modeling, thus reducing the number of motion reflective markers needed.[17,28,29]

Simulated environment was used to evaluate the accuracy of the FE-enrichment method in comparison to two commonly used surface approximation methods (**Figure 3**a), namely

© 2021 The Authors. Advanced Intelligent Systems published by Wiley-VCH GmbH

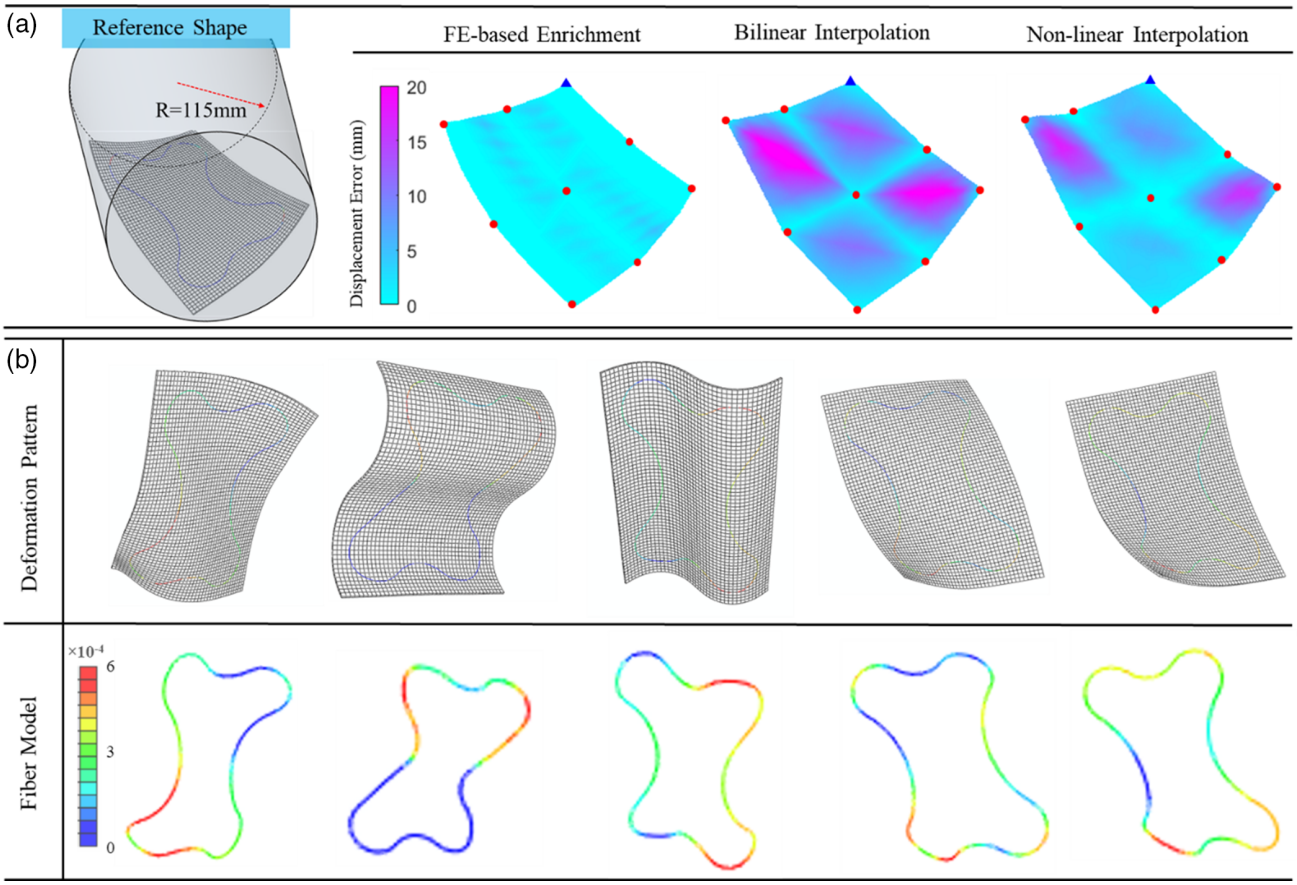

Figure 3. FE model and surface approximation. a) Surface reconstruction with three approximation methods based on nine tracked nodes, indicated as one blue triangle (fixed nodes) and eight red circles (free nodes). The displacement errors of piecewise bilinear interpolation, triangle-based nonlinear interpolation,[30] and FE-based data enrichment are color-coded with blue, indicating a smaller error. b) Fiber strain responses of five deformation patterns in FE simulation, where warmer colors indicate a higher induced strain.

bilinear and nonlinear interpolations. A virtual A4-sized sensor was placed on a reference cylinder object (with radius of $R = 115$ mm), which acted as the ground truth shape. Each method used the nine tracked sensor nodes as inputs/query points and displacement errors were calculated against the cylinder ground truth. The FE-enrichment method demonstrated a maximum displacement error of 3.2 mm, which outperformed the piecewise bilinear interpolation method (maximum error ≈19.7 mm) and triangle-based nonlinear surface interpolation (maximum error ≈16.8 mm).[30] The performance of the FE-based data enrichment method can be attributed to its use of the real sensor's geometric and material properties in the FE model.

The strain responses of various deformation patterns were also tested and compared (Figure 3b) with 3000 frames of simulated strain data and its corresponding displacement from FE simulation for model training. The overall error was small with a mean of 0.6995 mm, achieving a high goodness-of-fit with a correlation coefficient >0.999. The results support the feasibility of using a data-driven method to model the strain-morphology mapping prior to its real sensor fabrication, and the clear variation in fiber strains indicates that surface morphology could be well differentiated and thus reconstructed from the strain data.

2.3. Accuracy and Flexibility

The shape sensor flexibility was tested with various high-order deformation such that the surface nodes would undergo large displacements (Figure 1 and Video S1, Supporting Information). To evaluate shape sensing accuracy, 300 deformation instances were randomly selected to compare with the EM-tracked ground truth nodes. Note that such distinct deformation instances were not used in the previous model training. A histogram of 2700 nodal displacement errors (300 × 9 nodes) is shown in **Figure 4**a, which indicates that nearly 90% of the samples were well below 5 mm with a mean of 2.28 mm. The root-mean-square error (RMSE) of each tracked node and the fixed point (A7), with respect to their position on the sensor, is shown in Figure 4b,c. The warmer color of dots indicates a larger displacement sensing error. It can be observed that the prediction error of each node has a strong relationship with its distance to the fixed point and the mean displacement it underwent (Figure 4c). The nodes A1, K1, and K7 have the largest error, likely because they have a higher DoF, and therefore underwent larger displacement (Figure S2, Supporting Information).

© 2021 The Authors. Advanced Intelligent Systems published by Wiley-VCH GmbH

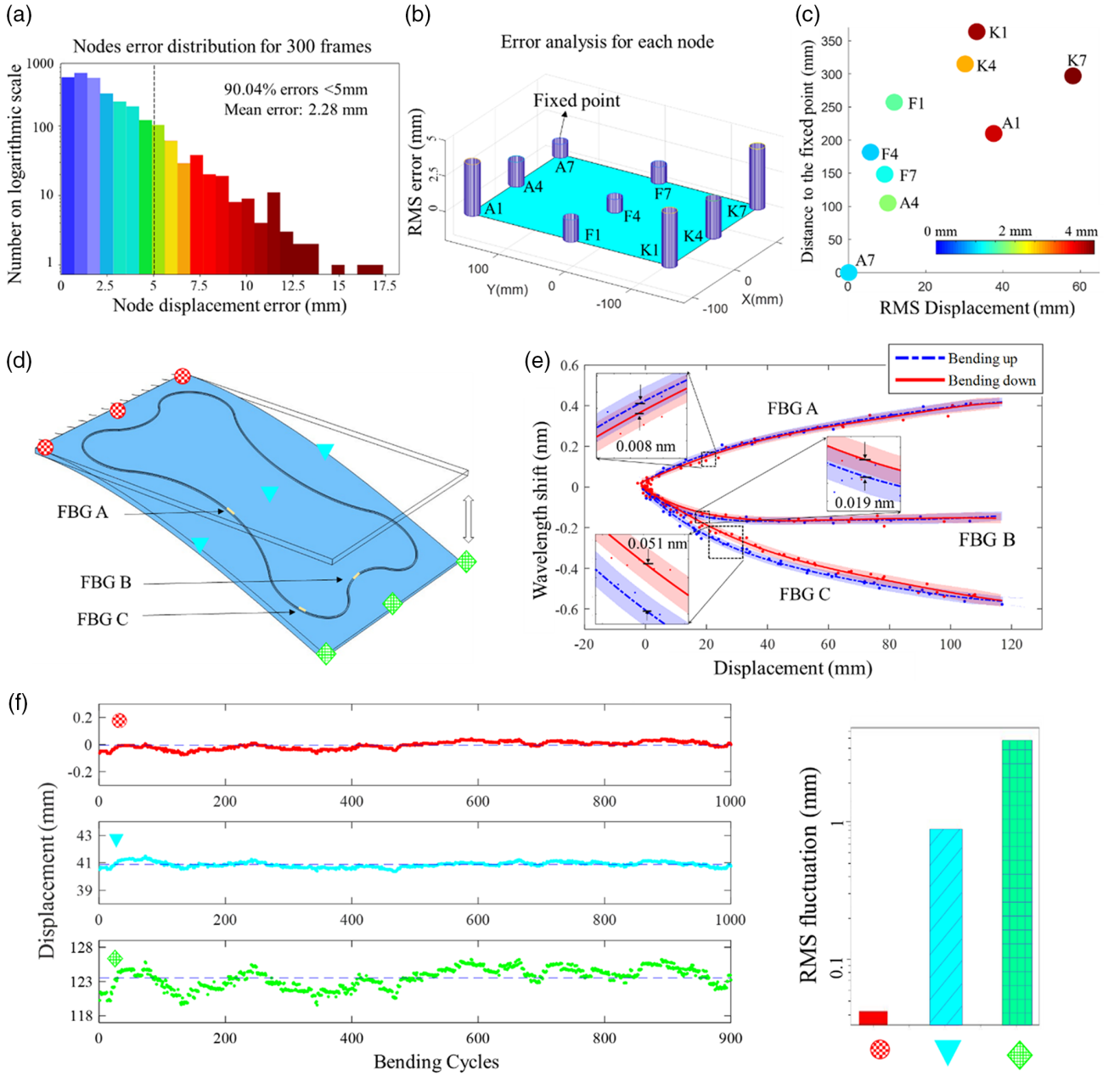

Figure 4. Accuracy, repeatability, and hysteresis analysis. a) Displacement error through 2700 node instances samples collected from 300 frames. b) The corresponding RMSE of each tracked node displacement. c) Error distribution compared with the distance from the fixed point (A7) and the node displacement. d) Setup for hysteresis and repeatability tests. The short edge of the shape sensor is clamped, with a linear actuator lifting the distal edge vertically. e) Hysteresis plot of three FBGs A, B, and C under bending cycles (0.5 Hz), by fitting curves through sampling points. f) Peak displacement of the three sides, i.e., the clamped side (red), the middle line (cyan), and the distal side (green). The sensor showed high repeatability during 1000 bending cycles. Quantitative comparison of the displacement fluctuation on a logarithmic scale (right).

2.4. Repeatability and Hysteresis

In this test, rather than only fixing a corner, a shorter edge of the shape sensor was clamped (Figure 4d), enabling a larger degree of deformation along the long edge. The sensor was bent upward, downward, then back to the neutral position, counting as one bending cycle. The bending motion was generated by a linear actuator driving the distal edge (nodes K1–K7) vertically, to conduct the sensing hysteresis test.

As shown in Figure 4e, three representative FBGs were selected, of which the Bragg wavelength shifts were read against the variation of distal edge displacement. Each data point was sampled by taking an average of three bending cycles. By fitting a curve along with those sampling points, the hysteresis could be

© 2021 The Authors. Advanced Intelligent Systems published by Wiley-VCH GmbH

measured as the disparity between the upward and downward bending, with the shadowed region representing the 95% confidence interval. Each hysteretic (or bending) cycle took around 2 s. These disparities could be varied, depending on the FBG locations. In general, they are very small (<0.051 nm), thus implying a low level of sensing hysteresis throughout such large bending cycles. To evaluate the longer term sensing repeatability, the displacements of three selected lines at the peak of upward motion were calculated and shown in Figure 4f. Altogether, the results suggest that the sensing was still promising with stable and reliable responses over 1000 repeated bending cycles. Again, this repeatability could also be varied by the displacement locations. The larger bending displacement detected by our shape sensor, the higher its fluctuation found over such repeated cycles. The fluctuation among those three lines of displacement nodes can be readily comparable on a logarithmic scale. Note that the nodes on the distal side encountered the largest fluctuation (RMS fluctuation ≈1.48 mm) as a result of its largest displacement detected.

2.5. Underwater Test

To further demonstrate the potential of our data-driven approach, we tested our training model in an underwater environment. A manta ray-shaped prototype was fabricated using the same settings of FBG fiber, following a similar procedure with the previous A4-sized design (Figure 4a). An optical fiber with 29 FBGs was adhered roughly along the edges of the prototype (**Figure 5a**), and its FE model is shown in Figure 5b, where the red nodes represent the location of eight EM tracking coils for the model training (ground truth).

The optical fiber layout for the manta ray prototype is not a dog-bone shape, but a specific one based on its geometry. When we were dealing with this case with irregular shape, we did not just simply copy the fiber layout from the rectangular one (A4-size). The middle fixture of the ray prototype has divided the substrate into two parts such that the resulting possible sensor configuration is fewer than that of the A4 size prototype. When displaced by hydrodynamic force, the deformation

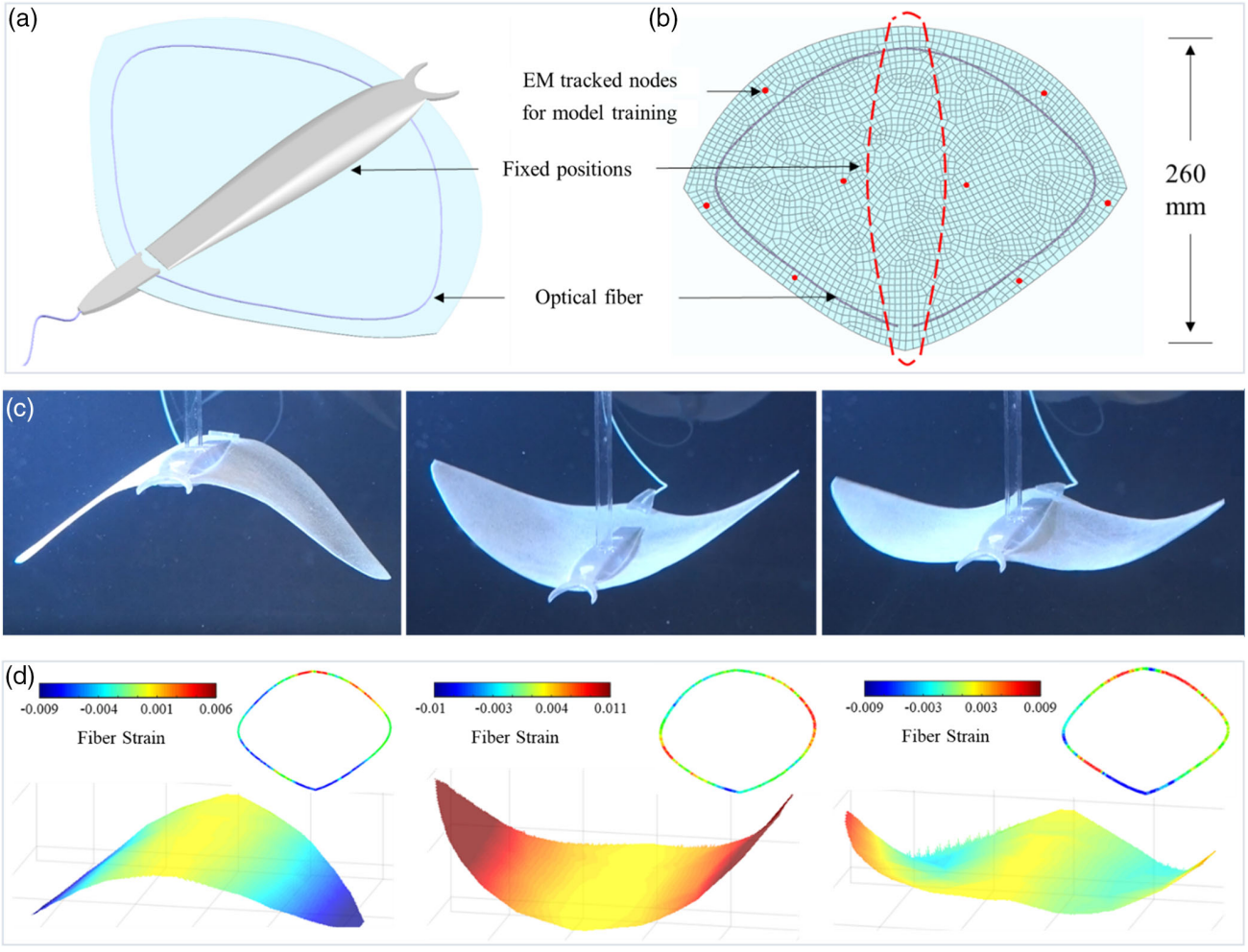

Figure 5. Shape sensing of underwater manta ray fin. a,b) Overview of the fin profile, with its FE model shown in (b). The soft fin made of silicone rubber was moved by a vertically actuated rod, interacting with continuous hydrodynamic forces. c,d) Three different phases of deformation poses and their corresponding shape reconstructed in real time as in (d) and Video S3, Supporting Information. Warmer the color, higher is the fiber strain induced along the fin contour. Note that the learning model training was conducted out of water beforehand. The unnoticeable deformation asymmetry can be reflected by its strains measured.

© 2021 The Authors. Advanced Intelligent Systems published by Wiley-VCH GmbH

magnitude and DoF of the fin edge are larger than that of the inner region. Therefore, we adhered the optical fiber along the edge of the manta ray prototype. Upon vertical actuation (1 Hz), the manta ray was displaced vertically underwater. The sensing performance of the manta ray fins can be referred to in Video S3, Supporting Information, as well as Figure 5, where Figure 5c shows the ray at three typical deformation instances and Figure 5d shows their corresponding real-time shape reconstruction. The ever-changing water drag did not hinder the sensing performance even with the model training and data-driven analysis initially conducted in the air.

3. Conclusion

In this work, we propose a sensor design framework that utilizes FE modeling for prefabrication parameter analysis and for the enrichment of sparse sensing data to achieve dense surface shape reconstruction. Through this approach, FE analysis allows us to overcome the typical requirement of having densely distributed grids of sensing elements to detect complex and high-resolution deformation information. We demonstrate the framework on a large (A4-sized), flexible, and thin (1 mm) surface shape sensor, with unprecedented sensing performance for complicated and large-scale morphology change. The shape sensor consists of a 1 mm-thick silicone substrate integrated with a single-core fiber containing 29 FBGs. Prior to fabrication, FE analysis was used to determine shape sensor parameters, namely, fiber placement in-depth, fiber layout pattern, and substrate thickness. FE analysis provides the ability to preemptively test the effect of modifying parameters without the need for extensive hardware prototyping. For example, the shape sensor parameters can be selected under intended deformation, such that the fiber strain would not reach its maximum allowable limit, thus protecting the fiber.

After fabrication, the shape sensor was trained through an ensemble learning method with the aid of an FE model for training data enrichment. Only nine locations/nodes on the surface shape sensor were used during ground truth data collection, where simultaneously the sensor was manually deformed in a single session (≈3 min). The combination of machine learning and FE-based data enrichment greatly relaxes the number of ground truth data needed because FE simulation could generate accurate and densely distributed data, and eases the need for precise fabrication and allocation of the sensing elements (i.e., FBGs). We also demonstrate that our FE modeling estimates more accurate intermediate data nodes based on the nine sparse nodes than piecewise bilinear interpolation and triangle-based nonlinear surface interpolation for surface reconstruction. The final trained shape sensor was able to reconstruct nodal displacements with an RMSE of 2.28 mm and an update frequency of 100 Hz. The mean peak displacement fluctuation of the distal side remained under 1.5 mm within 1000 repeated cycles, demonstrating reliability with little hysteresis found. Table S5, Supporting Information, shows that the proposed A4 shape sensor showed a competitive performance in comparison with some representative flexible surface sensors. A passive artificial ray sensor was also fabricated for underwater shape reconstruction, after its learning model was trained out of the water. This large-scale sensing framework could be applied to some bio-inspired robots, which have large and flexible wingspan. The FBG fiber or the sensing units could be embedded on surface of wings to predict the morphology of the robot, thus enabling closed-loop control.

In this work, we use sparse FBGs distributed along with a single-core optical fiber to measure local strain. The feasibility of this approach was also demonstrated by the shape sensing of other geometric designs. By attaching an optical fiber spirally to the surface of a soft continuum robot, valid 3D shape reconstruction of the tube-like structure can be obtained.[31] This spiral layout does not compromise the robot's flexibility while enabling shape sensing for closed-loop feedback. We believe this approach of direct installation can also be applied to a range of other soft robots.

Despite the capability in sensing and reconstructing the changes of high-order surface bending, allowable deformation of the presented prototype is still limited by axial stiffness of the underlying strain sensing elements (i.e., FBGs). Therefore, the sensing prototypes cannot tolerate the large in-plane stretching. However, with the advent of advanced stretchable sensing elements[32–34] (e.g., pressure, temperature,[35] curvature), rather than using optical FBGs. The gauge factor of FBG is 0.78, which is smaller than most of the silicone rubber-based stretchable strain sensors, for instance, 1.25[36] and 2.18.[37] The problem caused by conventional rigid wired connections could be solved with advances in microfluidics and flexible electronics (e.g., printed circuits filled with conductive liquid), which can overcome the limitations of flexibility and scalability. From this perspective, we believe our sensor design framework can also be implemented to achieve further enhanced multimodal sensing in flexible electronics, including bending, stretching, and pressing. As long as the local strain responses of those sensing elements can be differentiated across deformations, the proposed learning-based sensing framework can predict the morphological changes. Our method contributes by reducing the number of sensing units without sacrificing sensing capability. A sparse array with fewer connections is sufficient to achieve accurate real-time surface shape reconstruction, which requires denser sensing unit distribution by conventional approach. During this process, one indicator is the goodness-of-fit of training data, which reveals how well the strain-displacement mapping is regressed. In perspective of training data quality, this statistical value helps in judging whether the model is sensitive enough to distinguish sensor configuration.

4. Experimental Section

In this work, FBG fiber is chosen as the underlying sensing element due to its flexibility and ability to carry a high density of small strain sensors on a lightweight single fiber[36] with long-term stability.[37] It is worth noting that our framework is not limited to the use of FBGs, but can also be extended to other types of compact strain sensors proposed in the field of flexible electronics.[38,39] However, FBGs, as a handy choice for our framework validation, can measure high accuracy strain due to their nanoscale gratings which reflect the laser wavelengths that match the grating periods and transmit the remaining wavelengths. We used wavelength-division multiplexing (WDM)-based as opposed to the more complex and costly optical frequency domain reflectometry (OFDR)-based interrogation method. Although multicore and continuously written FBGs can be

© 2021 The Authors. Advanced Intelligent Systems published by Wiley-VCH GmbH

used with OFDR systems to calculate the 3D fiber curvature using analytical models, the model errors would be inevitably accumulated while applying integrals on the finite curvatures. Additional calibration and algorithmic error cancellation are required to ensure accurate curvature sensing. Moreover, the inherent update rate of OFDR systems[37] is usually lower (<100 Hz) than that of WDM (>1000 Hz), which would be insufficient in applications demanding high-frequency sensing feedback. When the grating period of an FBG is affected by axial strain, the corresponding wavelength components could be measured by the optical interrogator. The linear mathematical relationship between the wavelength shift $\Delta\lambda_m$ and mechanical strains ε_m could be expressed as

$$\varepsilon_m = \frac{1}{k}\left(\frac{\Delta\lambda_m}{\lambda_{0m}} - \frac{\Delta\lambda_c}{\lambda_{0c}}\right) \quad (1)$$

where λ_{0c} represents the central wavelength of compensation FBG, $\lambda_{0\,m}$ is the central wavelength of the FBG for mechanical strain, λ_c and λ_m are the corresponding wavelength shift, and $k = 0.78$ is the gauge factor.[40]

FE Modeling: To build a suitable FE model, the material properties of silicone rubber substrate and optical fiber are set in FE analysis software (Abaqus). We selected a silicone rubber with shore hardness A50, having considered other elastomeric alternatives in terms of their intrinsic flexibility and the capability to protect the inextensible optical fiber. Tensile tests were performed to determine the elastic modulus and the material properties of our selected silicone rubber with the use of digital image correlation (DIC) technique.[41] We used a standard testing procedure for rubber-like elastomer—American Society for Testing and Materials (ASTM) D412. During the test, the specimen was stretched incrementally at a uniaxial loading speed of 10 mm min^{-1}, while the specimen scanning was being conducted using a CCD camera at a frame rate of 10 Hz. By analyzing the stress–strain curve and the displacement fields, the elastic modulus and Poisson's ratio were determined to be 2.192 MPa and 0.393, respectively.

The silicone rubber body was set as a linear elastic 3D deformable part[42] and then meshed into $42 \times 60 \times 1$ eight-node brick elements ($\approx 5 \times 5 \times 1$ mm). Though being more computationally expensive than the standard eight-node brick element, additional incompatible displacement modes yield a more accurate bending response.[43] As for the optical fiber (Ø125 μm), the elastic modulus was set to 70 GPa with Poisson's ratio 0.1638 and then it was meshed into 85 two-node linear 3D truss elements (T3D2H). The geometric nonlinearity option, for small strain and large displacement, was chosen in the FE analysis. To simulate the sensor responses under varying loading conditions, one corner of the sensor was prescribed with the clamped condition while the rest is free. The fiber part was tied to the substrate surface with node region-to-surface constraint, and all FE simulations were done under static loading steps.

Sensor Design Parametrization: In the prototyping process, we investigated three important parameters using our FE simulation, namely, fiber placement in-depth, fiber layout pattern, and sensor thickness. Upon the FE analysis in our previous study,[19] the fiber strains magnitude would increase with its distance *l* from the neutral (middle) plane according to Kirchhoff plate theory, as shown in **Figure 6**a. To enhance sensitivity and minimize the sensor thickness, the fiber is positioned right below the surface plane. The off-center placement also guarantees the capability to distinguish bidirectional bending (Figure 6b), which could not be achieved if placing fiber at the neutral plane.[44]

The fiber layout pattern determines the distribution of FBG sensors, thereby substantially affecting the sensing capability of various morphologies. We proposed a dog-bone shape layout (Figure 2) with reference to similar designs,[17,45] and compared its strain response with two other primitive layouts, e.g., an ellipse and rounded rectangle (Figure S3, Supporting Information). Altogether, three typical sensor deformations were performed for our quantitative analysis in FE simulation. FBGs allocated in the dog-bone shape could cover close to the sensor regions involving a relatively higher degree of bending, such as the four corners and the central area of the A4-sized sensor. The dog-bone layout showed a smaller peak-to-peak strain range, which implies its potential to bear larger and more complicated deformation. The sensor thickness *t* would directly influence its flexibility, and it was decided by comparing a spectrum of thicknesses (0.2–4 mm), where the range is selected to avoid inhibiting the sensor or motion flexibility. The strain response pattern shown in Figure 6c is similar within the chosen thickness range, while the magnitude increases with the thickness. In addition, increasing the substrate thickness would result in the decrease in the flexibility of the sensor

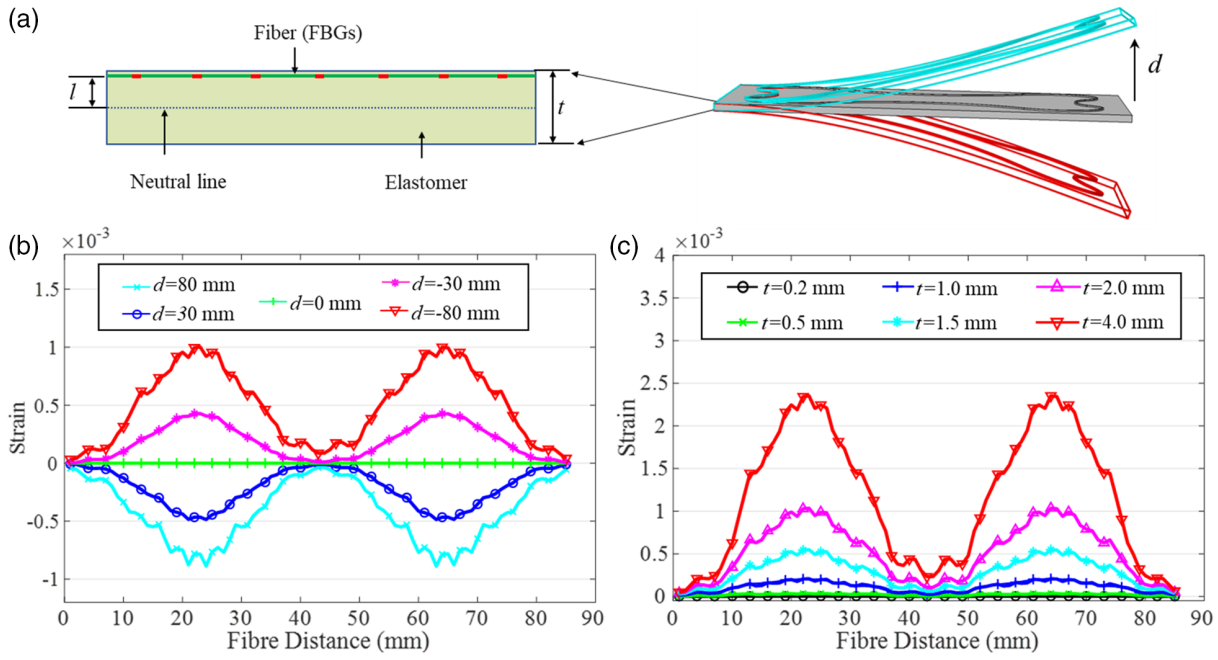

Figure 6. Sensor parameter analysis with FE simulation. a) A single-core fiber is adhered to silicone rubber with total thickness *t* under simple bending. The fiber is positioned away from the neutral plane with distance *l*. b) Simulated strain response of the FBGs when the free side of the sensor is bent with displacement *d* ranges from –80 to 80 mm. c) Simulation to compare the strain response of FBGs with thickness *t*, ranging from 0.2 to 4 mm.

© 2021 The Authors. Advanced Intelligent Systems published by Wiley-VCH GmbH

(e.g., the minimum bending radius). To strike a balance between flexibility and sensitivity, 1 mm thickness was finally chosen in our work.

Once the fiber layout and thickness were determined, the sensor was then fabricated using a 1 mm silicone rubber substrate with a hardness of Shore A50. A silicone adhesive (ELASTOSIL E41) is used to adhere the optical fiber and silicone rubber substrate. Each FBG has a length of 6 mm, with the spacing between adjacent FBGs being 22 mm for the first 28 FBGs. The 29th FBG is located 450 mm from the 28th FBG for the purpose of temperature compensation (Figure S4, Supporting Information). The fiber was tightly adhered to the substrate so that it can measure the surface strain of the substrate. The sensor prototype can be seen in Video S4, Supporting Information. Although the FBG distribution does not directly cover the entire shape sensor surface, any local deformation occurring at the corner or the edge will generate strain responses in individual gratings proximal to the deformation location. When provided with larger, nonlocal deformations, it is expected to generate global strain responses.

During the fabrication process, it is challenging to precisely position the FBG sensors on a designated path due to the fiber thinness and translucence. This fabrication error would pose challenges to kinematics model, and also demand additional calibration steps for error compensation, particularly with an irregular fiber layout. Therefore, we introduce a data-driven method to train the mapping from the sparse strain data to the dense morphology, but without prior knowledge regarding the actual location of FBGs along the elastomer surface.

Ensemble Learning Configuration: To reconstruct the surface morphology, a unique model mapping from the sparse strain data to surface deformation is needed. Conventional mathematical methods, in general, require highly accurate sensor fabrication or error compensation steps and can become exceedingly complex for high-dimensional problems such as morphology reconstruction. In contrast, data-driven methods such as machine learning approaches are suited to systems with modeling problems that are nonlinear, impractical, or impossible to represent analytically.[3,46,47] In our work, a mapping from sparse strains to dense displacements is formulated and regressed by a data-driven model. This approach bypasses the requirement for precise fabrication processes, allowing for the use of unique and irregular fiber layouts and FBG allocations, overall providing greater freedom in sensor customization and design. Namely, our approach leverages the use of sliding windows and ensemble learning to improve predictive performance while maintaining high-frequency calculation for such a high-dimensional regression problem.[48,49]

In this A4-sized prototype, we divided the rectangular sensor surface into multiple smaller rectangular regions/windows with fixed width and height (Figure 2), where the nodes inside the same window would have a strong spatial correlation. Each window had an individual submodel and covered the same amount of output nodes, and some nodes were included in multiple regions. Each submodel (ANN-based predictor) was responsible for processing the surface nodes inside the corresponding window, with all submodels sharing the same input data, i.e., all of the strain data (Video S5, Supporting Information). The overlapped region of windows would result in multiple calculations of some nodal data, thus enhancing the prediction robustness. In addition, by dividing the surface into smaller regions, the spatial correlation between adjacent points under continuous deformation could be leveraged, resulting in higher prediction accuracy. Finally, a complete model can be ensembled upon the weighted voting results of all independent regressors.[50–52]

Supporting Information

Supporting Information is available from the Wiley Online Library or from the author.

Acknowledgements

Research reported in this article was supported by the Research Grants Council (RGC) of Hong Kong (grant nos. 17207020, 17206818, 17205919, and T42-409/18-R) and the Innovation and Technology Commission (ITC) (grant no. UIM/353). *The Interactive Supporting Information of this article can be found at*: https://authorea.com/doi/full/10.22541/au.162255864.44424722/v3.

Conflict of Interest

The authors declare no conflict of interest.

Data Availability Statement

Research data are not shared.

Keywords

computational mechanics, ensemble learning, flexible sensors, robotic proprioception, surface shape sensing

Received: May 7, 2021
Revised: June 30, 2021
Published online: August 30, 2021

[1] G. Soter, A. Conn, H. Hauser, J. Rossiter, in *IEEE Inter. Conf. Robot. Autom. (ICRA)*, Brisbane, Australia **2018**, pp. 2448–2453.
[2] H. Wang, M. Totaro, L. Beccai, *Adv. Sci.* **2018**, *5*, 1800541.
[3] K. Chin, T. Hellebrekers, C. Majidi, *Adv. Intell. Syst.* **2020**, *2*, 1900171.
[4] C. Laschi, B. Mazzolai, M. Cianchetti, *Sci. Robot.* **2016**, *1*, 1.
[5] S. Sareh, Y. Noh, M. Li, T. Ranzani, H. Liu, K. Althoefer, *Smart Mater. Struct.* **2015**, *24*, 125024.
[6] B. Shih, D. Shah, J. Li, T. G. Thuruthel, Y.-L. Park, F. Iida, Z. Bao, R. Kramer-Bottiglio, M. T. Tolley, *Sci. Robot.* **2020**, *5*, eaaz9239.
[7] T. Hoshi, H. Shinoda, in *IEEE SICE Annu. Conf.*, Tokyo, Japan **2008**, pp. 915–920.
[8] A. Hermanis, R. Cacurs, M. Greitans, *IEEE Sens. J.* **2016**, *16*, 1271.
[9] A. Hermanis, K. Nesenbergs, in *13th IEEE Biennial Baltic Electron. Conf. (BEC)*, Tallinn, Estonia **2012**, pp. 203–206.
[10] T. Hoshi, S. Ozaki, H. Shinoda, in *4th Inter. Conf. Networked Sensing Syst.*, Association for Computing Machinery, New York, NY **2007**, pp. 207–212.
[11] P. Mittendorfer, G. Cheng, in *IEEE/RSJ Inter. Conf. Intell. Robots Syst. (IROS)*, Vilamoura, Algarve **2012**, pp. 4505–4510.
[12] N. Saguin-Sprynski, L. Jouanet, B. Lacolle, L. Biard, in *Eur. Workshop Structural Health Monit. (EWSHM)*, Nantes, France **2014**, pp. 702–709.
[13] A. F. D. Silva, A. F. Goncalves, P. M. Mendes, J. H. Correia, *IEEE Sens. J.* **2011**, *11*, 2442.
[14] S. Rapp, L.-H. Kang, U. C. Mueller, J.-H. Han, H. Baier, in *Proc. SPIE*, **2007**, *6529*, 65293E.
[15] H. Zhang, X. Zhu, Z. Gao, K. Liu, F. Jiang, *J. Intell. Mater. Syst. Struct.* **2016**, *27*, 2416.
[16] L. Xu, J. Ge, J. H. Patel, M. P. Fok, in *Opt. Fiber Commun. Conf. Exhib. (OFC)*, Los Angeles, CA **2017**, pp. 1–3.
[17] C. Rendl, D. Kim, S. Fanello, P. Parzer, C. Rhemann, J. Taylor, M. Zirkl, G. Scheipl, T. Rothländer, M. Haller, in *Proc. ACM symp. User Interface Softw. Technol. (UIST)*, New York, NY **2014**, pp. 129–138.
[18] I. M. Van Meerbeek, C. M. De Sa, R. F. Shepherd, *Sci. Robot.* **2018**, *3*, eaau2489.
[19] T. L. T. Lun, K. Wang, J. D. L. Ho, K. Lee, K. Y. Sze, K. Kwok, *IEEE Robot. Autom. Lett. (RA-L)*. **2019**, *4*, 1454.
[20] D. Marinkovic, M. Zehn, *Appl. Sci.* **2019**, *9*, 2775.

© 2021 The Authors. Advanced Intelligent Systems published by Wiley-VCH GmbH

[21] A. Mendizabal, P. Márquez-Neila, S. Cotin, *Med. Image Anal.* **2020**, *59*, 101569.
[22] F. Roewer-Despres, N. Khan, I. Stavness, presented at *15th Int. Symp. Comput. Methods Biomechan. Biomed. Eng. (CMBBE)*, March **2018**, p. 1.
[23] K.-H. Lee, D. K. Fu, M. C. Leong, M. Chow, H.-C. Fu, K. Althoefer, K. Y. Sze, C.-K. Yeung, K.-W. Kwok, *SoRo.* **2017**, *4*, 324.
[24] R. Haferssas, P. Jolivet, F. Nataf, *SIAM J. Sci. Comput.* **2017**, *39*, A1345.
[25] G. Li, X. Chen, F. Zhou, Y. Liang, Y. Xiao, X. Cao, Z. Zhang, M. Zhang, B. Wu, S. Yin, Y. Xu, *Nature.* **2021**, *591*, 66.
[26] S. Aracri, F. Giorgio-Serchi, G. Suaria, M. E. Sayed, M. P. Nemitz, S. Mahon, A. A. Stokes, SoRo. January **2021**, Epub ahead of print, https://doi.org/10.1089/soro.2020.0011.
[27] A. Ramezani, S. J. Chung, S. Hutchinson, *Sci. Robot.* **2017**, *2*, 3.
[28] M. K. Dobrzynski, R. Pericet-Camara, D. Floreano, in *IEEE/RSJ Inter. Conf. Intell. Robots Syst. (IROS)*, San Francisco, CA **2011**, pp. 1913–1918.
[29] F. Saunders, E. Golden, R. D. White, J. Rife, *Robotica* **2011**, *29*, 823.
[30] S. Cuomo, A. Galletti, G. Giunta, L. Marcellino, *Appl. Math. Sci.* **2014**, *8*, 6717.
[31] X. Wang, G. Fang, K. Wang, X. Xie, K. H. Lee, J. D. Ho, W. L. Tang, J. Lam, K. W. Kwok, *IEEE Robot. Autom. Lett.* **2020**, *5*, 2161.
[32] J. Byun, Y. Lee, J. Yoon, B. Lee, E. Oh, S. Chung, T. Lee, K.-J. Cho, J. Kim, Y. Hong, *Sci. Robot.* **2018**, *3*, eaas9020.
[33] H. Bai, S. Li, J. Barreiros, Y. Tu, C. R. Pollock, R. F. Shepherd, *Science* **2020**, *370*, 848.
[34] O. A. Araromi, M. A. Graule, K. L. Dorsey, S. Castellanos, J. R. Foster, W.-H. Hsu, A. E. Passy, J. J. Vlassak, J. C. Weaver, C. J. Walsh, *Nature.* **2020**, *587*, 219.
[35] M. Behl, K. Kratz, U. Noechel, T. Sauter, A. Lendlein, *Proc. Natl. Acad. Sci.* **2013**, *110*, 12555.
[36] X. Guo, Y. Huang, Y. Zhao, L. Mao, L. Gao, W. Pan, Y. Zhang, P. Liu, *Smart Mater. Struct.* **2017**, *26*, 095017.
[37] P. Liu, W. Pan, Y. Liu, J. Liu, W. Xu, X. Guo, C. Liu, Y. Zhang, Y. Ge, Y. Huang, *Compos. Sci. Technol.* **2018**, *159*, 42.
[38] B. A. Childers, M. E. Froggatt, S. G. Allison, T. C. Moore, Sr. D. A. Hare, C. F. Batten, D. C. Jegley, *SPIE's 8th Annu. Inter. Symp. Smart Struct. Mater.* **2001**, *4332*, 133.
[39] M. Amanzadeh, S. M. Aminossadati, M. S. Kizil, A. D. Rakić, *Measurement.* **2018**, *128*, 129.
[40] W. Gao, H. Ota, D. Kiriya, K. Takei, A. Javey, *Acc. Chem. Res.* **2019**, *52*, 523.
[41] S. Huang, Y. Liu, Y. Zhao, Z. Ren, C. F. Guo, *Adv. Funct. Mater.* **2019**, *29*, 1805924.
[42] M. Kreuzer, HBM, Darmstadt, S2338-1.0 e. **2006**, p. 12.
[43] R. H. Pritchard, P. Lava, D. Debruyne, E. M. Terentjev, *Soft Matter.* **2013**, *9*, 6037.
[44] D. Coric, M. Lai, J. Botsis, A. Luo, H. G. Limberger, *Opt. Express* **2010**, *18*, 26484.
[45] A. J. Sadowski, J. M. Rotter, *Int. J. Mech. Sci.* **2013**, *74*, 143.
[46] J. Ge, A. E. James, L. Xu, Y. Chen, K.-W. Kwok, M. P. Fok, *IEEE Photon. Technol. Lett.* **2016**, *28*, 2237.
[47] H. Hocheng, C.-M. Chen, *Sensors.* **2014**, *14*, 11855.
[48] H. Drucker, C. J. Burges, L. Kaufman, A. Smola, V. Vapnik, *Adv. Neural. Inf. Process Syst.* **1997**, *9*, 155.
[49] A. Liaw, M. Wiener, *R News* **2002**, *2*, 18.
[50] O. Sagi, L. Rokach, *Wiley Interdiscip. Rev. Data Min. Knowl. Discov.* **2018**, *8*, e1249.
[51] L. Breiman, *Mach. Learn.* **1996**, *24*, 123.
[52] Y. L. Park, B. R. Chen, R. J. Wood, *IEEE Sens. J.* **2012**, *12*, 2711.

© 2021 The Authors. Advanced Intelligent Systems published by Wiley-VCH GmbH